METTL1 Mediated m^{7}G Modification Regulates Ferroptosis and Chemotherapy Resistance via Involvement of pri-miR-26a/FTH1 Axis in Osteosarcoma

Ye Yuan (yuanye_hmu@126.com)
Department of Pharmacy,the Second affiliated hospital of Harbin Medical University

Mingyu He
Harbin Medical University

Yang Wang
Harbin Medical University

Jiaying Pu
Harbin Medical University

Zhihua Shen
Harbin Medical University

Tong Wang
Harbin Medical univesity

Guanghui Li
Harbin Medical University

Zhongting Mei
Harbin Medical University

Ao Wang
Harbin Medical University

Zijing Ren
Harbin Medical University

Ying Liu
Harbin Medical University

Wenbo Wang
The First Affiliated Hospital of Harbin Medical University

Xiaoyan Liu
The First Affiliated Hospital of Harbin Medical University

Hong Lei
Harbin Medical University

Xiaoqi He
Harbin Medical University

Qian Liu
Harbin Medical University

Jinhuan Hong
Harbin Medical University

Weijie Du
Harbin Medical University

Lei Yang
Harbin Medical University

Research

Keywords: Osteosarcoma, m7G methylation, METTL1, FTH1, pri-miR-26a, ferroptosis, chemotherapy resistance

Posted Date: November 10th, 2021

DOI: https://doi.org/10.21203/rs.3.rs-1003392/v1

Abstract

Background

N7-Methyladenosine (m7G), one of the most prevalent internal modifications in mammalian RNAs, makes a great contribution to many bioprocesses. However, its functions and underlying mechanisms in the occurrence and development of osteosarcoma remain elusive.

Methods

The expression of METTL1 and its correlation with clinicopathological features using tissue microarrays and the Cancer Genome Atlas (TCGA) dataset.Targets of METTL1 on osteosarcoma were identified by AlkAniline-seq, RNA immunoprecipitation (RIP), quantitative real-time PCR, western blot and luciferase assays. The effects of METTL1 on the biological characteristics of osteosarcoma cells were investigated on the basis of gain- and loss-of-function analyses. Ferroptosis were analyzed by lipid peroxidation assay, iron assay and ransmission electron microscopy (TEM). Subcutaneous models further uncovered the role of METTL1 in tumour growth.

Results

Here, we have identified that METTL1, an m7G methyltransferase, is low expressed in osteosarcoma tissues and plays an antitumor role in osteosarcoma. Mechanistically, METTL1 enhances cell ferroptosis by targeting pri-miR-26a and promoting its mature through m7G methylation, which could target FTH1 mRNA and eliminate FTH1 translation efficiency mediated by METTL1. FTH1 is the main component of ferritin which is crucial for iron homeostasis and the inhibition of lipid peroxidation. Reduction of FTH1 translation dramatically increases ferroptosis and enhances osteosarcoma chemosensitivity.

Conclusions

Collectively, our study demonstrates the METTL1/pri-miR-26a/FTH1 axis signaling in osteosarcoma and highlights the functional importance of METTL1 and m7G methylation in the progression and chemotherapy resistance of osteosarcoma, suggesting that reprogramming RNA m7G methylation as a potential and promising strategy for osteosarcoma treatment.

Background

Osteosarcoma is one of the most common malignant tumors of bone which occurs in children and adolescents under the age of 20 characterized by a high risk of metastatic progression and recurrence [1]. Despite the advances in chemotherapy and surgery, the 5-year survival rate still remains unchangeable for decades, as localized osteosarcoma was 70%, whereas metastatic osteosarcoma drops drastically to 30% [2]. Thus, exploration of molecular mechanism underlying the development and progression of osteosarcoma is urgent for developing novel therapeutic strategies.

Emerging evidence has showcased the potency of epigenetic regulations for controlling the tumorigenesis and development of diverse human cancers, including DNA methylation [3], histone acetylation [4], and N^6-methyladenosine (m^6A) [5]. Recently, we and others have discovered the connectivity between m^6A methylation, one of the most hotspots in RNA modification, with tumor progression via dynamic regulation of m^6A-methylated RNA transcripts [6,7]. Besides, N^7-methylguanosine (m^7G) is also one of the most abundant modifications presenting in transfer RNA (tRNA) variable loop [8], eukaryotic 18S ribosomal RNA (rRNA) [9], microRNA (miRNA) [10], and mRNA 5'cap [11] and that may impact the biological regulation of RNA processing. m^7G methylation is catalyzed by methyltransferase like 1 (METTL1) and WD repeat domain 4 (WDR4) complex in mammals and METTL1 is responsible for catalyzing methylation, while WDR4 makes a great contribution to stabilizing the methyltransferase complex [12]. Recent studies have suggested that m^7G modification in mRNAs or non-coding RNAs plays critical roles in stem cell self-renewal

and differentiation [12–14] and post-ischemic angiogenesis [15]. Besides, previous researchs have observed that the dysregulation of METTL1 mediated m^7G modification is functionally correlated with the development and prognosis of colon, liver, breast cancer, and intrahepatic cholangiocarcinoma [16–20]. Given the known crucial role of METTTL1 in tumors, characterizing the effects involved in osteosarcoma and clarifying the underlying mechanism has become a focus of intensive study.

Ferroptosis is an iron-dependent form of regulated cell death driven by excessive lipid peroxidation, of which morphology and mechanism is distinct from cell apoptosis [21]. Generally, glutathione (GSH)-dependent selenoenzyme glutathione peroxidase 4 (GPX4) is deemed essential for preventing ferroptosis via reducing toxic lipid hydroperoxides to nontoxic lipid alcohol [22,23]. Emerging studies have proved that ferroptosis plays an extremely critical antitumor role in diverse cancers, including pancreatic cancer [24], gastric cancer [25], glioblastoma [26] and so on. Moreover, triggering ferroptosis enhanced drug-resistant cancer cells sensitivity to chemotherapeutic drugs such as cisplatin, temozolomide, and doxorubicin [27–29], indicating that induction of ferroptosis can potentially be a novel and effective strategy in cancer treatment.

Materials And Methods

Cell lines and cell culture

Human osteosarcoma cell line U2OS and human embryonic kidney (HEK) 293T cells were maintained in Dulbecco`s modified Eagle medium (DMEM) (Life Technologies Corporation, California, USA) supplemented with 10% fetal bovine serum (FBS) (Biological Industries, Israel). 143B and 143B/Luc were cultivated in MEM/EBSS basic medium (HyClone, Utah, USA) supplemented with 10% FBS (Biological Industries, Israel). All cell lines were maintained in an incubator at 37°C in an atmosphere containing 5% CO_2. All cells were repeatedly screened for mycoplasma and maintained in culture for < 6 months after receipt.

Cell transfection

Cells were transfected to knock down the expression of METTL1 and AMO-miR-26a-5p using Lipofectamine TM 3000 Transfection Reagent (Cat# L3000-015; Invitrogen, California, USA). METTL1, FTH1, FTH1-mut plasmid and miR-26a-5p mimic were purchased from Gene Pharma (China) to increase the expression of the plasmid. Briefly, for siRNAs, 2×10^5 cells were seeded in a 6-well plate and they will be 70% confluent at the time of transfection 6 μL Lipofectamine TM 3000 reagent and 20 nM siRNA (Gene Pharma, Shanghai, China) were diluted in 125 μL Opti-MEM (Cat# 31985-070; gibco, Grand Island, USA) medium respectively. After Mix and incubating for 2 min separately, these two regents were then mixed and incubated for another 10 min and then added to cells. For plasmids, cells were transfected with 500 ng plasmid using Lipofectamine™ 3000 Transfection Reagent according to the manufacturers' protocols. Subsequent experimental measurements were performed 24 h after transfection.

The sequences used are as following:

METTL1 siRNA sense: 5’-CCAAAGGAUAAGAAAGAAATT-3’

METTL1 siRNA antisense: 5’-UUUCUUUCUUAUCCUUUGGTT-3’

AMO-MiR-26a-5p: 5’-AGCCUAUCCUGGAUUACUUGAA-3’

hsa-miR-26a-5p mimics sense: 5’-UUCAAGUAAUCCAGGAUAGGCU-3’

hsa-miR-26a-5p mimics antisense: 5’-AGCCUAUCCUGGAUUACUUGAA-3’

Invasion assay

Matrigel invasion assay was performed using 24 well plates inserted by 24 mm Transwell® chambers (Corning #3412, USA) precoated with Matrigel (BD Biosciences, San Jose, CA). 5×10^4 cells were resuspended in 200 μL Serum-free medium, seeded into the upper chamber, and medium containing 10% FBS was added into the bottom chamber subsequently. After incubation at

37℃ for 24 h, cells on the underside of the membrane were immobilized and stained with 0.1% crystal violet (Beyotime Biotechnology, China) for 15 min and counted using light microscopy (ECLIPSE TS100, Nikon).

Colony-formation assay

Cells transfected with targeted siRNA or plasmid were seeded in 6 well plates with a concentration of 1,500 cells per well and suspended in the media with 10% FBS. The indicated cells cultured in a humidi□ed atmosphere containing 5% CO_2 at a constant temperature of 37℃ to form colonies for 14 days. Colonies were stained with 0.1% crystal violet for 20 min after fixation with 10% formaldehyde for 5 min. Different colony morphologies were captured under a light microscope (ECLIPSE TS100, Nikon).

Cell Counting Kit-8 (CCK8) assay

Cell viability and growth were determined using CCK8 assay in 96 well plates. Cells were transfected with the relevant plasmids culturing for 24 h, followed by incubation with 10 μL CCK8 for 90 min. Absorbance was read at 450 nm using a spectrophotometer (Tecan, Männedorf, Switzerland).

Migration assay

Cells were plated into 6 well plates at a density of 2.5×10^5 cells/mL. When the confluence of cells reached 70%, a wound was created by scraping the cells with a 200 μL pipette tip. Cells were washed with phosphate-buffered saline (PBS) and then transfected with siRNAs or plasmid. Images were captured at 0 h, 24 h, and 48 h after wounding with standard light microscopy (ECLIPSE TS100, Nikon, Japan). The wound area was measured using ImageJ software (National Institutes of Health, USA).

Alkaline hydrolysis and aniline cleavage sequencing (AlkAniline-seq)

The m^7G AlkAniline-Seq sequencing service was provided by CLOUDSEQ (Shanghai cloud-seq biomart, http://www.cloud-seq.com.cn). Alkaline hydrolysis of poly (A) -enriched mRNA fragments were used. Cells were incubated with thermosensitive phosphatase (NewEnglandBiolabs, Inc. USA) to dephosphorylate RNA sheet pairs, followed by incubation and lysis in 1 M aniline. RNA libraries were constructed using NEBNext® MultiplexSmallRNALibraryPrepSetforIllumina ® (NewEnglandBiolabs, Inc., USA) according to the supplier's instructions, and library quality control and quantification were performed using the BioAnalyzer2100 system (Agilent Technologies, USA). High-throughput sequencing was performed using an IlluminaHiSeq sequencer.

Quantitative real-time polymerase chain reaction (qRT-PCR)

Total RNA was extracted using TRIZOL reagent (Life Technologies Corporation) followed the manufacturer's protocol. 500 ng total RNA was reverse-transcribed into 10 μL cDNA using High Capacity cDNA Reverse Transcription Kit (Cat#00676299; Thermo Fisher Scientific, Waltham, USA). qRT-PCR analysis was needed 1 μL cDNA, 1 μL forward primer, 1 μL reverse primer, and SYBR Green PCR Master (Cat#31598800; Roche) by a 7500 Fast Real-Time instrument (Applied Biosystems, Foster City, USA). Gene expression was normalized to endogenous GAPDH. The miRNA amplified transcript level was normalized to U6. Primer sequences can be found in Additional file file: Table S1.

Ethynyl-2-deoxyuridine (EdU) staining assay

EdU Apollo DNA *in vitro* kit (Ribobio, Guangzhou, China) was used to detect cell proliferation. Cells were plated into 24 well plates (NEST, Hong Kong, China) at a density of 2×10^5. Briefly, cells were fixed with 4% paraformaldehyde (m/v) for 30 min and followed by incubation of 30 μM/mL EdU at 37℃ for 90 min. After permeabilized in 0.5% Triton X-100, the Apollo staining solution was added into the cell culture medium for 30 min in the dark. Finally, the cells were incubated with 20 μg/mL 4',6-diamidino-2-phenylindole (DAPI) for 10 min. The EdU index (%) was the average ratio of the number of EdU positive cells over total cells in five randomly selected areas under the confocal laser scanning microscope (FV10i, Olympus, Tokyo, Japan).

Tissue microarrays (TMAs) and Immunohistochemistry (IHC) analysis

Osteosarcoma tissue microarrays were purchased from the Bioaitech Company (Xi'an, China), comprised of 11 normal bone tissues, 70 malignant osteosarcoma cores. The slide was baked at 60℃ for 30 min and then followed by antigen retrieval with tris-EDTA buffer (pH 9.0), medium heat for 10 min to boil, cease-fire for 5 min, and washed with PBS for 5 min × 3 times.

Endogenous peroxidase was blocked with 3% H_2O_2-methanol at RT for 25 min and washed with PBS for 5 min × 3 times. The sections were added to normal non-immune animal serum at RT for 10 min and then removed the serum and added different primary antibodies FTH1 (#4393, CST), 4-HNE (bs6313R, Bioss), Ki67 (27309-1-AP, Protein tech), METTL1 (14994-1-AP, protein tech) at 4℃ overnight. Then it was washed with 0.1% tween-20 PBS for 5 min × 3 times. Biotin-labeled sheep anti-mouse/rabbit IgG was added and incubated in a 37℃ wet box for 30 min followed by washing with 0.1 % tween-20 PBS for 5 min × 3 times. DAB working solution was incubated for 5 min and stopped by distilled water washing. After hematoxylin re-staining, washing and differentiation, the slide returned to be blue with full washing followed with regular dehydration transparent and being sealed by neutral gum. The percentage of positive cells were counted in 5 (×400) highpower fields (upper, lower, left, right, and middle) under the microscope, and the mean values were then calculated.

RNA immunoprecipitation (RIP)-qPCR

RIP assay was carried out in 143B cells using Magna RIP Kit (17-700, Millipore, MA) following the manufacturer's instructions. In brief, a sufficient number of 143B cells (more than 2 × 10^7 cells per sample) were lysed by RIP lysis buffer, magnetic beads pre-coated with 5 μg m^7G antibody or mouse IgG (Millipore) were incubated with sufficient cell lysates at 4℃ overnight. The mixture was digested with proteinase K before the immunoprecipitated RNAs were extracted, purified and subjected to qPCR. The RNA levels were normalized to the input RNA levels (10%).

RNA stability assay

Cells were cultured in 6 well plates and transfected with desired constructs as described above. After 24 h transfection, cells were treated with actinomycin D (Act D, 10 μg/mL, Cat# GC16866, GLPBIO) for 0 h, 3 h, 6 h and 9 h before collection. Total RNAs were isolated for qRT-PCR analysis.

Iron assay

Cells were cultured in a 6 well plate, after 24 h transfection, cell precipitation was collected, the intracellular ferrous iron level using an iron assay kit from ScienCell (8448, California, USA). The absorbance was finally measured at 590 nm.

Luciferase reporter assay

The luciferase reporter assay was performed with the Dual-Luciferase (Promega E2920) according to the manufacturer's protocol. HEK-293T cells seeded in 24 well plates were transfected with a SV40-firefly-Luciferase-MCS fused the wild-type FTH1, miR-26a-5p mimics or NC were co-transfected. Firefly luciferase activity was normalized to Renilla luciferase activity to reflect transfection efficiency.

Lipid peroxidation assay

The relative lipid peroxidation level in cells was assessed using the Image-iT® Lipid Peroxidation Kit (molecular probes, C10445). Cells were treated with 5 μM C11-BODIPY for 30 min harvested, washed twice with PBS and resuspended in 500 μL PBS. Oxidation of the polyunsaturated butadienyl portion of the dye results in a shift of the fluorescence emission peak from 590 nm to 510 nm.

Xenograft tumorigenesis model

BABL/c female nude mice were purchased from Beijing Vital River Laboratory Animal Technology Limited Company (Beijing, China) and randomized into two groups. All animal experiments were performed in accordance with protocols approved by the Animal Care and Use Committee of Harbin Medical University. Mice were injected subcutaneously with 5 × 10^6 143B cells to form subcutaneous xenografts. Mouse tumor growth was monitored by measuring tumor length as well as width. Mice weights in each group were recorded accordingly. When tumors grew to a volume of 200 mm^3, the mice were divided randomly into six groups (n = 5/group) and treated with normal saline, 1 mg/kg Dox (Doxorubicin hydrochloride, MCE, HY15142), 1 mg/kg Fer-1 (Ferrostatin-1, MCE, HY100579, ferroptosis inhibitor), vehicle by daily intraperitoneal administration, body weights of mice in each group during treatment were also recorded accordingly, the animals were sacrificed four weeks after 143B cell transplantation. Xenograft sampling was performed, and tumor volume was calculated by the standard formula: (length ×

width^2)/2. Before xenograft sampling, the xenografts were anesthetized with isoflurane gas, scanned with an IVIS *in vivo* imaging system (IVIS LuminaIII, MA, USA), and the total photon radiation at each tumor site was quantified using Living Image software. Mice were euthanized for xenograft sampling.

Transmission electron microscopy

After the cells were pretreated accordingly, the cells were mixed and centrifuged for 250 revolutions for 5 min. Discard the culture medium, add 1 mL PBS culture medium, and resuspend the cells. Next, the samples were horizontally centrifuged at 3000 rpm for 20 min. After the completion of centrifugation, PBS was discarded, and 2.5% glutaraldehyde was added to fix the cells. Cells were dehydrated with an ethanol concentration gradient and embedded in resin. They were then sectioned with an ultramicrotome, stained with uranyl acetate-lead citrate double staining, and finally observed under a transmission electron microscope.

Western Blot

Cell samples were washed using PBS, and then the total proteins were extracted using 1×RIPA lysis buffer (Beyotime, Shanghai, China). The lysates were fully crushed by ultrasonic and cleared by high-speed centrifugation at 13,500g for 15 min. The extracted total proteins were quantified by BCA Protein Assay Kit (Beyotime, Shanghai, China), then equal amounts of proteins were separated by SDS-PAGE and transferred to NC membrane. After the membranes were blocked with 5% w/v non-fat milk for 1h, the proteins were probed at 4℃ overnight using different primary antibodies METTL1 (14994-1-AP, proteintech), FTH1 (#4393, CST), GPX4 (A13309, Abclonal), GAPDH (AC002, Abclonal), β-Tubulin (AC021, Abclonal). On the next day, the membranes were incubated with a secondary antibody (RS23910, ImmunoWay) for 1 h at room temperature. Results were detected using Odessey Clex (LI-COR, America), followed by further analysis.

Hematoxylin and Eosin Staining (H&E) staining

The H&E staining Kit (G1120, Solarbio) was used for H&E staining, paraffin sections were stained with hematoxylin for 5 min and differentiated with differentiation solution for 30 s, followed by soaking into tap water for 15 min. And then the sections were stained with eosin, followed by dehydrated with gradient alcohol and cleared with xylene. Images were acquired using a Leica microscope and Leica image software.

Statistical analysis

All experiment results were at least repeated three times and expressed as means ± SEM. Statistical analyses were performed using GraphPad Prism 8.0 and Student's T-test was used for two-group comparisons. $p < 0.05$ was considered statistically significant. *P < 0.05; **P < 0.01; ***P < 0.001.

Results

Elevated METTL1 expression correlates with a good prognosis of patients with osteosarcoma

We initially used immunohistochemistry (IHC) assays to detected METTL1 protein expression levels in osteosarcoma tissues from 71 patients with osteosarcoma from tissue microarrays (TMAs) and 20 normal bone tissues (Figure 1A and Additional file 1: Figure S1). METTL1 expression was significantly lower in osteosarcoma tissues than that in normal bone tissues, which was further decreased with the higher clinical stage (Figure 1B). Kaplan–Meier analysis using data derived from the TCGA cohort also revealed that high expression of the METTL1 was associated with a good prognosis in patients with sarcoma (Figure 1C).

FTH1 is the target gene of METTL1 identified by AlkAniline-Seq

To identify potential targets of METTL1 the m^{7}G methylation levels of which are regulated by METTL1, we conducted alkaline hydrolysis and aniline cleavage sequencing (AlkAniline-Seq) in 143B cells, a human osteosarcoma cell line (Figure 2A). AlkAniline-Seq data revealed that 45,048 m^{7}G methylated sites ≥ 2 folds decrease in METTL1 silencing group compared with those in negative control (NC) group, and of those, 2,047 m^{7}G methylated sites counts were greater than or equal to 50, which

had 150 m^7G methylated sites counts greater than or equal to 100 in NC group (Figure 2B). We listed the top 10 genes with the most significant changes in methylation sites (Table 1), among those m^7A abundances of ferritin heavy chain 1 (FTH1), myosin ID (MYO1D), and Disks Large Homolog 2 (DLG2) were the most markedly decreased upon METTL1 knockdown (Figure 2C). Considering that METTL1 has been proved to promote m^7G modification of mRNA as a methyltransferase and to facilitate RNA synthesis [30], we hypothesized that FTH1, MYO1D, and DLG2 are potential targets of METTL1. Furthermore, METTL1 knockdown in 143B cells resulted in a significant downregulation of FTH1, MYO1D, and DLG2 mRNA, while overexpression of METTL1 led to a notable upregulation of FTH1 and MYO1D mRNA, except DLG2 (Figure 2D and 2E). However, FTH1 exhibited the most consistent decreased m^7G level and mRNA level in METTL1 knockdown 143B cells versus that of the NC group. We next performed gene-specific m^7G qPCR assays for FTH1 and confirmed the m^7G level decrease in FTH1 transcript, demonstrating the reliability of our transcriptome-wide AlkAniline-Seq data (Figure 2F). FTH1 has ferroxidase activity and is involved in iron accumulation which is important for iron homeostasis [31]. Kaplan–Meier analysis exhibited that sarcoma patients with low expression of the FTH1 have a longer survival time (Figure 2G). To further explore the potential mechanism of METTL1 regulating FTH1 mRNA expression, we treated NC or METTL1 knockdown 143B cells with the transcription inhibitor actinomycin D (Act D) and detected the half-life of FTH1 transcripts. As expected, METTL1 silencing indeed resulted in a remarkable decrease in the half-life of FTH1 transcripts (3.85 to 14.84 h, Figure 2H).

Table 1
Top 10 mRNAs

No.	Gene symbol	Chrom	m^7G position	Strand	Fold change (siNC/siMETTL1)
1	**FTH1**	**chr11**	**61,732,268**	**-**	**94.93**
2	**MYO1D**	**chr17**	**31,149,715**	**-**	**42.86**
3	**DLG2**	**chr11**	**85,195,218**	**-**	**39.15**
4	VAC14	chr16	70,812,179	-	25.54
5	KIAA0226L	chr13	46,948,706	-	24.30
6	RPL17-C18orf32	chr18	47,015,637	-	16.84
7	RPL17	chr18	47,015,637	-	16.84
8	TAF1D	chr11	93,466,672	-	16.66
9	MYO1D	chr17	31,149,461	-	11.16
10	GNL3	chr3	52,726,787	+	10.51

METTL1 decrease FTH1 protein level via positively regulating the combination of miR-26a-5p and FTH1 mRNA

A previous study has demonstrated that internal m^7G methylation regulated by METTL1 could promote mRNA translation[11]. Surprisingly, forced expression METTL1 in 143B cells significantly reduced FTH1 protein levels (Figure 3A), indicating that there may be other underlying mechanisms for FTH1 post-transcriptional regulation. AlkAniline-Seq dates showed that METTL1 knockdown also has led to a noticeable reduction of m^7G methylated sites in pri-miRNA, while 4,278 m^7G methylated sites decreased 2 folds compared to the NC group, and 65 of these sites decreased counts greater than or equal to 50 in the NC group (Figure 3B). Notably, among the top 20 genes with the most significant changes, pri-miR-26a and pri-miR-98 were highly conserved (Table 2). In addition, METTL1 knockdown in 143B cells reduced the expression of pri-miR-26a, while overexpression of METTL1 resulted in a significant upregulation of pri-miR-26a (Figure 3C). However, the expression of pri-miR-98 was too low to be detected (data not shown) and METTL1 had no significant effect on the expression of miR-98 (Figure 3D). Of note,

METTL1 positively regulated the mature of miR-26a-5p indicating that METTL1 might regulate the miRNA biogenesis by m^7G modification (Figure 3D). To establish the cause of the decrease in FTH1 protein levels,anti-miR-26a-5p oligonucleotide (AMO) or miR-26a-5p mimics were transfected in 143B cells. This revealed a significant increase or decrease in the expression of FTH1 in miR-26a-5p AMO or mimics groups respectively, at protein levels rather than mRNA levels compared to the respective control cells (Figure 3E and 3F). It indicated that miR-26a-5p might target FTH1 and regulate FTH1 translation. To further verify whether FTH1 is the target of miR-26a-5p, HEK-293T cells were co-transfected with miR-26a-5p mimics or NC mimics and FTH1 luciferase vectors. Dual-luciferase reporter assay showed that the luciferase activity of the FTH1 mRNA was markedly reduced in the group transfected with miR-26a-5p mimics (Figure 3G). Collectively, METTL1 both increases the m^7G modification and the expression of FTH1 mRNA and pri-miR-26a, and further substantially promotes miR-26a-5p mature which could bind to FTH1 mRNA and eliminate the improvement of FTH1 translation efficiency (Figure 3H).

Table 2
Top 20 primary-miRNAs

No.	Pri-miRNA	Chrom	m^7G position	Fold changes (siNC/siMETTL1)	No.	Pri-miRNA	Chrom	m^7G position	Fold changes (siNC/siMETTL1)
1	miR-663b	chr2	133,012,018	37.67	11	miR-3134	chr3	15,839,158	3.00
2	miR-6850	chr8	146,016,833	13.83	12	miR-548au	chr9	96,339,948	3.00
3	miR-4804	chr5	72,204,866	3.00	13	miR-548v	chr8	17,502,162	3.00
4	miR-558	chr8	32,694,511	3.00	**14**	**miR-98, let-7f-2**	chrX	**53,674,403**	**3.00**
5	miR-4685	chr10	100,176,928	3.00	15	miR-4637	chr5	14,711,390	3.00
6	miR-6877	chr9	135,933,800	3.00	16	miR-3128	chr2	178,117,579	3.00
7	miR-6830	chr5	131,528,561	3.00	17	miR-1908	chr11	61,569,097	3.00
8	**miR-26a-1**	chr3	**38,025,680**	**3.00**	18	miR-548as	chr13	93,131,606	3.00
9	miR-6834	chr6	33,258,655	3.00	19	miR-1301	chr2	25,463,593	3.00
10	miR-3161	chr11	48,023,350	3.00	20	miR-4779	chr2	86,389,164	3.00

METTL1 suppresses cell viability of human osteosarcoma cells via inducing ferroptosis

We then performed gain- and loss-of-function studies to elucidate the pathological role of METTL1 in 143B and U2OS cells, two human osteosarcoma cell lines, and the transfection efficiency was detected by western-blot (Additional file 1: Figure S2A and S2B). The cell proliferation was analyzed using CCK-8 assay, EdU staining, and clone formation. All these results showed that 143B and U2OS cell proliferative capability was dramatically decreased following METTL1 overexpression (Figure 4A-4C). The cell invasion and migration rate were also obviously abrogated by forced expression of METTL1 through transwell assay and wound-healing assay (Figure 4D and 4E). Conversely, knockdown of METTL1 in 143B cells slightly promoted cell proliferation and invasion ability (Additional file 1: Figure S3A and S3B).

Given that METTL1 regulates m^7G methylation modification of FTH1, which is crucial for labile iron pool stabilization, we next elucidated the function of METLL1 in ferroptosis. We used C11BODIPY staining to detected lipid peroxidation in 143B and U2OS cells after transfected with or without METTL1 plasmids. C11BODIPY staining showed obvious lipid peroxidation in response to METTL1 overexpression (Figure 5A). Ferrostatin-1 (Fer-1), a synthetic antioxidant, is known to be a specific ferroptosis inhibitor inhibiting lipid peroxidation. Consistently, 4 h pretreatment with Fer-1 clearly abrogated METTL1-induced lipid peroxidation (Figure 5A). The morphological characteristics of ferroptosis in transmission electron microscopy (TEM) include dense and small mitochondria, increased membrane density, and cristae degeneration[21]. To identify these morphological features, we performed TEM evaluation in 143B cells. Dense and shrunken mitochondria were remarkably apparent in the METTL1 overexpression group compared to the control group, which could be reversed by Fer-1 treatment (Figure 5B). Similarly, METTL1 overexpression also dramatically increased iron accumulation, while Fer-1 could abolish this phenomenon (Figure 5C). Nevertheless, there was no noticeable change of the protein level of glutathione peroxidase 4 (GPX4), an intrinsic negative regulator for lipid peroxidation and ferroptosis, after METTL1 overexpression both in 143B and U2OS cells (Additional file 1: Figure S4). Moreover, METTL1 overexpression further intensified the inhibition effect of ferroptosis inducer RAS-selective lethality 3 (RSL3) on cell viability (Figure 5D). In particular, Fer-1 significantly alleviated METTL1 overexpression induced cell proliferation inhibition as measured by EdU staining assay in 143B and U2OS cells, respectively (Figure 5E). The involvement of ferroptosis in METTL1 induced cell viability inhibition was further supported by the negligible effects of the pan-caspase inhibitor Z-VAD-FMK and the necroptosis inhibitor necrostatin-1 (Nec-1) treatment on cell proliferation inhibition caused by METTL1 overexpression (Additional file 1: Figure S5). Taken together, these data suggests that ferroptosis is predominantly responsible for the inhibition of cell viability caused by METTL1 overexpression.

Fer-1 eliminates tumor growth inhibition resulted by METTL1 *in vivo*

To assess METTL1 gain of function, we constructed stably METTL1 overexpression and control 143B luciferase cell line via lentivirus transfection and used it to establish animal xenograft model (Figure 6A). METTL1 overexpression group mice were randomly divided into 2 groups, one of which was given Fer-1 by intraperitoneal injection on day 10 (Figure 6A), the time we exactly observed tumor formation and average radiance values of both the METTL1 group and prepared for the Fer-1 group were slightly lower than the control group (Additional file 1: Figure S6). The average radiance value detected by *in vivo* imaging, tumor weight, and tumor volume indicated noticeable retardation of tumor growth resulted by METTL1 overexpression, which was gradually and dramatically reversed by Fer-1 (Figure 6B-6E). Similarly, these treatment effects were further supported by hematoxylin and eosin (H&E) staining as well as Ki67 immuno-staining on tissue sections from the differently treated groups (Figure 6F). Interestingly, IHC staining of lipid peroxidation marker 4-hydroxynonenal (4-HNE) levels showed that METTL1 could considerably induce the production of 4-HNE, while Fer-1 treatment significantly decreased the expression of 4-HNE (Figure 6F).

miR-26a-5p is involvement in the ferroptosis and cell viability inhibition modulated by METTL1

Considering the m^7G methylation of miR-26a-5p modified by METTL1, we then asked whether miR-26a-5p affects METTL1-mediated ferroptosis and antitumor function. TEM of bronchial epithelial cells was examined in 143B cells. Apparently, accumulation of mitochondria with increased membrane density was presented in the METTL1 overexpression group, which was barely detected in the co-transfected group containing METTL1 plasmids and miR-26a-5p AMO (Figure 7A). Furthermore, miR-26a-5p silencing also remarkably eliminated the excessive iron levels and lipid peroxidation production caused by METTL1 overexpression (Figure 7B and 7C). Given that miR-26a-5p could target FTH1 and regulated its translation (Figure 3E), we examined the translation regulation of the FTH1 association between METTL1 and miR-26a-5p. Of note, the miR-26a-5p inhibitor significantly enhanced the protein level of FTH1 reduced by METTL1 overexpression. Consistently, miR-26a-5p silencing both reversed cell proliferation inhibition of 143B and U2OS cells regulated by METTL1 overexpression (Figure 7E). Taken together, these results indicated that the involvement of miR-26a-5p in METTL1-mediated ferroptosis and cell viability inhibition is at least partially via post-transcriptional regulation of FTH1.

METTL1-mediated ferroptosis increases sensitivity to chemotherapy both *in vitro* and *in vivo*

The above results prompted us to ask whether METTL1-mediated ferroptosis and antitumor function are sufficient to cause anti-drug resistance. To this end, we analyzed the expression of METTL1 in human osteosarcoma cell lines treated with chemotherapy agents both doxorubicin (Dox) and cisplatin (Cis). Obviously, these drugs significantly decreased the mRNA expression of METTL1 in the 143B and U2 OS cell lines as well as protein levels (Figure 8A and 8B). To explore the potential role of METTL1 in osteosarcoma cells sensitivity to chemotherapy, we transfected METTL1 plasmids into 143B and U2OS cells with 24 h treatments of Dox or Cis. We found that METTL1 overexpression in these cells rendered them noticeably more sensitive to Dox and Cis-induced cell injury associated with proliferation inhibition (Figure 8C-8F). Accumulating evidence has demonstrated the roles of Dox or Cis in ferroptosis [32,33]. Interestingly, METTL1 overexpression could exacerbate the lipid peroxidation production and iron accumulation led by Dox and Cis treatment, which can be partially prevented with Fer-1 treatment (Figure 8G-8J).

To further explored the function of METTL1 on chemosensitivity of osteosarcoma cells *in vivo*, the BALB/c nude mice were subcutaneously transplanted with 143B tumor cells transfected with lentivirus. Mice were then treated with Dox beginning at day 10 (Figure 9A). Tumors derived from the mice cotreated with empty lentivirus and Dox grew more slowly compared with those derived from empty lentivirus transfected, which could be further alleviated by lentivirus-mediated METTL1 overexpression, both in weight and volume (Figure 9B-9E). Consistent with these results, H&E staining and Ki67 immuno-staining further demonstrated that METTL1 overexpression promoted chemosensitivity of osteosarcoma bearing nude mice (Figure 9F). Moreover, ectopic expression of METTL1 along with Dox treatment dramatically enhanced 4-HNE production indicating that METTL1-mediated ferroptosis is involved in the chemotherapy resistance inhibition (Figure 9F).

Discussion

Starting from the observation of METTL1 negatively correlated with the clinical stage of osteosarcoma, we here demonstrated that METTL1 overexpression can impede osteosarcoma progression and improve osteosarcoma chemosensitivity via targeting pri-miR-26a/FTH1 axis in an m^7G methylation manner. Specifically speaking, our study for the first time found that METTL1 positively regulates FTH1 methylation modification and further maintains its transcript stabilization. Meanwhile, METTL1 can promote miR-26a maturity by increasing its precursor pri-miR-26a methylation level that can offset translation efficiency of FTH1 promoted by METTL1-mediated m^7G methylation. Attenuating the expression of FTH1 protein restrains the accumulation of iron and the production of lipid peroxidation in osteosarcoma cells, which subsequently induces ferroptosis and inhibits chemotherapy resistance (Figure 10).

Accumulating studies has demonstrated that dysfunction of METTL1 is associated with a range of disorders. For instance, ribosome pausing at m^7G-tRNA dependent codons caused by METTL1/WDR4 complex mutation impairs embryonic stem cells proliferation and neural differentiation [12]. METTL1-mediated m^7G modification of vascular endothelial growth factor A (VEGFA) significantly promotes mice post-ischemic angiogenesis *in vivo* as well as human umbilical vein endothelial cells angiogenesis increased *in vitro* [15]. Interestingly, recent several studies also observed that METTL1-mediated m^7G tRNA modification drives oncogenic mRNA which promotes leukemia [34] and intrahepatic cholangiocarcinoma progression [20]. Conversely, METTL1 was identified to have antitumor activity via regulating let-7e miRNA/HMGA2 axis in an m^7G dependent manner [16]. Consistently, our study for the first time proved that METTL1 is positively correlated with the prognosis of osteosarcoma patients.

The AlkAniline-Seq assay and the subsequent validation and functional studies suggest that FTH1 is the critical target gene of METTL1. FTH1, a key component of ferritin, plays a vital role in ferroptosis defense by sequestering redox-active iron [35]. FTH1 has been reported to participate in the physiological process of brain injury [36], Parkinson's disease [31], and cardiomyopathy [35]. Moreover, degradation of FTH1 exhibited antitumor activity in leukemia by reducing lipid peroxides content and further restoring cell ferroptosis [37]. However, whether FTH1-mediated ferroptosis is involved in osteosarcoma progression is still largely unknown. As an m^7G RNA methyltransferase, METTL1 enhances the m^7G level of FTH1, which in turn leads to the upregulation at the RNA

level via promoting its stabilization. Our study differs from the previous observation that METTL1-mediated m^7G modification in mammalian mRNA increases translation efficiency [11,30], whereas our dates indicate that overexpression of METTL1 significantly decreases the FTH1 protein level. A possible explanation for this apparent discrepancy is that METTL1 is known to have abundant cellular regulatory targets.

Interestingly, by further analyzing of AlkAniline-Seq dates and validation studies, we revealed that METTL1 deficiency dramatically reduces the mature of miR-26a-5p via m^7G methylation, which has been reported to act as a tumor suppressor in osteosarcoma [38,39]. METTL1-mediated m^7G position has been identified to be essential for let-7e stem-loop equilibrium and thereby promotes its processing, which can further selectively regulate the translation of oncogenic mRNAs in hepatoma carcinoma cells [10]. Consistently, our data showed miR-26a-5p combines with FTH1 transcript promoting FTH1 translation. Attenuation of FTH1 protein caused by METTL1 overexpression dramatically enhances lipid peroxidation production and induces cell ferroptosis which could be abrogated by ferroptosis inhibitor Fer-1 both *in vivo* and *in vitro*. Simultaneously, miR-26a-5p silencing reverses the inhibition of FTH1 protein and blocks the occurrence of ferroptosis resulted by forced expression of METTL1.

Despite the development of multiple chemotherapy brought tremendous changes to the improvement of osteosarcoma patients' overall survival, the great challenge of overcome drug resistance in osteosarcoma treatment is still unchanged over the past decades [40]. Doxorubicin, cisplatin, and methotrexate are the first-line chemotherapy drugs applied for osteosarcoma treatment [41]. A recent study has demonstrated that METTL1 overexpression promoted chemosensitivity of colon cancer cells to cisplatin by regulating miR-149-3p/S100A4/p53 axis [18]. Our dates indicate that METTL1 expression was negatively regulated by doxorubicin and cisplatin in osteosarcoma cells, whereas METTL1 overexpression significantly improved the efficacy of doxorubicin and cisplatin via the increasement of ferroptosis.

Collectively, our studies demonstrate the critical role of METTL1 in the development and chemosensitivity of osteosarcoma, as featured by inducing lipid peroxidation and promoting ferroptosis of osteosarcoma cells, and uncover a previously unrecognized signaling axis involving METTL1/pri-miR-26a/FTH1 in osteosarcoma. Moreover, our study highlights the functional importance of the m^7G modification mediated by METTL1 in osteosarcoma and provides profound insights into the molecular mechanisms underlying tumorigenesis in osteosarcoma. In addition, given the functional importance of METTL1 in leukemogenesis and drug response, targeting METTL1 signaling by selective promotors may represent a promising therapeutic strategy to treat osteosarcoma, especially in METTL1-low patients.

Abbreviations

Act D: actinomycin D; AlkAniline-seq: aniline cleavage sequencing; Cis: cisplatin; DLG2: Disks Large Homolog 2; Dox: doxorubicin; Fer-1: Ferrostatin-1; FTH1: ferritin heavy chain 1; GPX4: glutathione peroxidase 4; IHC: Immunohistochemistry; METTL1: methyltransferase like 1: m^7G: N^7-Methyladenosine: miRNA: microRNA; MYO1D: myosin ID; Nec-1: necrostatin-1; Tissue microarraysTMAs: Tissue microarrays; 4-HNE: 4-hydroxynonenal.

Declarations

Ethics approval and consent to participate

Written informed consent was obtained from all participants in accordance with the Declaration of Helsinki. All the collection of specimens and animal handling in this study was reviewed and approved by the Medical Ethics Committee of the First Affiliated Hospital of Harbin Medical University (KY2018-185).

Consent for publication

Not applicable.

Availability of data and materials

Not applicable.

Competing interests

The authors declare that they have no competing interests.

Funding

This work was supported by grants from the National Natural Science Fund of China (81972117), the Natural Science Foundation of Heilongjiang Province of China for outstanding youth (YQ2020H019), Natural Science Foundation of Heilongjiang Province of China for excellent youth (JJ2020JQ0004), the First Affiliated Hospital of Harbin Medical University Excellent Young Talents Funding (HYD2020JQ0013), Special fund for clinical research of Wu Jieping Medical Foundation (320.6750.2020-04-50), CAMS Innovation Fund for Medical Sciences (CIFMS, 2020-I2M-5-003), and HMU Marshal Initiative Funding (HMUMIF-21009)

Author Contributions

Y.Y., M.H., and Y.W. together with J.P., Z.S., Y.L., W.W. X.L. H.L. and X.H. performed *in vitro* assays. Y.Y., T.W., G.L., Z.M., A.W. and Z.R. contributed to the *in vivo* animal experiments. L.Y., W.D and Y.Y. designed experiments and supervised the study. Y.Y., M.H., and Y.W. analyzed and interpreted data. Y.Y. and L.Y. wrote the draft, and all of the authors revised and approved the final manuscript.

Acknowledgements

Not applicable.

References

1. Mirabello, L. *et al.* Frequency of Pathogenic Germline Variants in Cancer-Susceptibility Genes in Patients With Osteosarcoma. *JAMA Oncol* **6**, 724-734, doi:10.1001/jamaoncol.2020.0197 (2020).
2. Lallier, M. *et al.* Molecular Chaperones in Osteosarcoma: Diagnosis and Therapeutic Issues. *Cells* **10**, doi:10.3390/cells10040754 (2021).
3. Segovia, C. *et al.* Inhibition of a G9a/DNMT network triggers immune-mediated bladder cancer regression. *Nat Med* **25**, 1073-1081, doi:10.1038/s41591-019-0499-y (2019).
4. Shen, S. M. *et al.* PTENalpha and PTENbeta promote carcinogenesis through WDR5 and H3K4 trimethylation. *Nat Cell Biol* **21**, 1436-1448, doi:10.1038/s41556-019-0409-z (2019).
5. Li, Z. *et al.* FTO Plays an Oncogenic Role in Acute Myeloid Leukemia as a N(6)-Methyladenosine RNA Demethylase. *Cancer Cell* **31**, 127-141, doi:10.1016/j.ccell.2016.11.017 (2017).
6. Yuan, Y. *et al.* ALKBH5 suppresses tumor progression via an m(6)A-dependent epigenetic silencing of pre-miR-181b-1/YAP signaling axis in osteosarcoma. *Cell Death Dis* **12**, 60, doi:10.1038/s41419-020-03315-x (2021).
7. Li, J. *et al.* YTHDF2 mediates the mRNA degradation of the tumor suppressors to induce AKT phosphorylation in N6-methyladenosine-dependent way in prostate cancer. *Mol Cancer* **19**, 152, doi:10.1186/s12943-020-01267-6 (2020).
8. Lin, S., Liu, Q., Jiang, Y. Z. & Gregory, R. I. Nucleotide resolution profiling of m(7)G tRNA modification by TRAC-Seq. *Nat Protoc* **14**, 3220-3242, doi:10.1038/s41596-019-0226-7 (2019).
9. Letoquart, J. *et al.* Structural and functional studies of Bud23-Trm112 reveal 18S rRNA N7-G1575 methylation occurs on late 40S precursor ribosomes. *Proc Natl Acad Sci U S A* **111**, E5518-5526, doi:10.1073/pnas.1413089111 (2014).
10. Pandolfini, L. *et al.* METTL1 Promotes let-7 MicroRNA Processing via m7G Methylation. *Mol Cell* **74**, 1278-1290 e1279, doi:10.1016/j.molcel.2019.03.040 (2019).
11. Zhang, L. S. *et al.* Transcriptome-wide Mapping of Internal N(7)-Methylguanosine Methylome in Mammalian mRNA. *Mol Cell* **74**, 1304-1316 e1308, doi:10.1016/j.molcel.2019.03.036 (2019).

12. Lin, S. *et al.* Mettl1/Wdr4-Mediated m(7)G tRNA Methylome Is Required for Normal mRNA Translation and Embryonic Stem Cell Self-Renewal and Differentiation. *Mol Cell* **71**, 244-255 e245, doi:10.1016/j.molcel.2018.06.001 (2018).
13. Deng, Y., Zhou, Z., Ji, W., Lin, S. & Wang, M. METTL1-mediated m(7)G methylation maintains pluripotency in human stem cells and limits mesoderm differentiation and vascular development. *Stem Cell Res Ther* **11**, 306, doi:10.1186/s13287-020-01814-4 (2020).
14. Deng, Y., Zhou, Z., Lin, S. & Yu, B. METTL1 limits differentiation and functioning of EPCs derived from human-induced pluripotent stem cells through a MAPK/ERK pathway. *Biochem Biophys Res Commun* **527**, 791-798, doi:10.1016/j.bbrc.2020.04.115 (2020).
15. Zhao, Y. *et al.* m7G Methyltransferase METTL1 Promotes Post-ischemic Angiogenesis via Promoting VEGFA mRNA Translation. *Front Cell Dev Biol* **9**, 642080, doi:10.3389/fcell.2021.642080 (2021).
16. Liu, Y., Zhang, Y., Chi, Q., Wang, Z. & Sun, B. Methyltransferase-like 1 (METTL1) served as a tumor suppressor in colon cancer by activating 7-methyguanosine (m7G) regulated let-7e miRNA/HMGA2 axis. *Life Sci* **249**, 117480, doi:10.1016/j.lfs.2020.117480 (2020).
17. Tian, Q. H. *et al.* METTL1 overexpression is correlated with poor prognosis and promotes hepatocellular carcinoma via PTEN. *J Mol Med (Berl)* **97**, 1535-1545, doi:10.1007/s00109-019-01830-9 (2019).
18. Liu, Y. *et al.* Overexpressed methyltransferase-like 1 (METTL1) increased chemosensitivity of colon cancer cells to cisplatin by regulating miR-149-3p/S100A4/p53 axis. *Aging (Albany NY)* **11**, 12328-12344, doi:10.18632/aging.102575 (2019).
19. Okamoto, M. *et al.* tRNA modifying enzymes, NSUN2 and METTL1, determine sensitivity to 5-fluorouracil in HeLa cells. *PLoS Genet* **10**, e1004639, doi:10.1371/journal.pgen.1004639 (2014).
20. Dai, Z. *et al.* N(7)-Methylguanosine tRNA modification enhances oncogenic mRNA translation and promotes intrahepatic cholangiocarcinoma progression. *Mol Cell*, doi:10.1016/j.molcel.2021.07.003 (2021).
21. Dixon, S. J. *et al.* Ferroptosis: an iron-dependent form of nonapoptotic cell death. *Cell* **149**, 1060-1072, doi:10.1016/j.cell.2012.03.042 (2012).
22. Friedmann Angeli, J. P. *et al.* Inactivation of the ferroptosis regulator Gpx4 triggers acute renal failure in mice. *Nat Cell Biol* **16**, 1180-1191, doi:10.1038/ncb3064 (2014).
23. Yang, W. S. *et al.* Regulation of ferroptotic cancer cell death by GPX4. *Cell* **156**, 317-331, doi:10.1016/j.cell.2013.12.010 (2014).
24. Tang, R. *et al.* The role of ferroptosis regulators in the prognosis, immune activity and gemcitabine resistance of pancreatic cancer. *Ann Transl Med* **8**, 1347, doi:10.21037/atm-20-2554a (2020).
25. Zhang, H. *et al.* CAF secreted miR-522 suppresses ferroptosis and promotes acquired chemo-resistance in gastric cancer. *Mol Cancer* **19**, 43, doi:10.1186/s12943-020-01168-8 (2020).
26. Yee, P. P. *et al.* Neutrophil-induced ferroptosis promotes tumor necrosis in glioblastoma progression. *Nat Commun* **11**, 5424, doi:10.1038/s41467-020-19193-y (2020).
27. Liu, Q. & Wang, K. The induction of ferroptosis by impairing STAT3/Nrf2/GPx4 signaling enhances the sensitivity of osteosarcoma cells to cisplatin. *Cell Biol Int* **43**, 1245-1256, doi:10.1002/cbin.11121 (2019).
28. Buccarelli, M. *et al.* Inhibition of autophagy increases susceptibility of glioblastoma stem cells to temozolomide by igniting ferroptosis. *Cell Death Dis* **9**, 841, doi:10.1038/s41419-018-0864-7 (2018).
29. Fu, J. *et al.* Activatable nanomedicine for overcoming hypoxia-induced resistance to chemotherapy and inhibiting tumor growth by inducing collaborative apoptosis and ferroptosis in solid tumors. *Biomaterials* **268**, 120537, doi:10.1016/j.biomaterials.2020.120537 (2021).
30. Boulias, K. & Greer, E. L. Put the Pedal to the METTL1: Adding Internal m(7)G Increases mRNA Translation Efficiency and Augments miRNA Processing. *Mol Cell* **74**, 1105-1107, doi:10.1016/j.molcel.2019.06.004 (2019).
31. Tian, Y. *et al.* FTH1 Inhibits Ferroptosis Through Ferritinophagy in the 6-OHDA Model of Parkinson's Disease. *Neurotherapeutics* **17**, 1796-1812, doi:10.1007/s13311-020-00929-z (2020).

32. Liu, Y. *et al.* Acyl-CoA thioesterase 1 prevents cardiomyocytes from Doxorubicin-induced ferroptosis via shaping the lipid composition. *Cell Death Dis* **11**, 756, doi:10.1038/s41419-020-02948-2 (2020).
33. Hu, Z. *et al.* VDR activation attenuate cisplatin induced AKI by inhibiting ferroptosis. *Cell Death Dis* **11**, 73, doi:10.1038/s41419-020-2256-z (2020).
34. Orellana, E. A. *et al.* METTL1-mediated m(7)G modification of Arg-TCT tRNA drives oncogenic transformation. *Mol Cell*, doi:10.1016/j.molcel.2021.06.031 (2021).
35. Fang, X. *et al.* Loss of Cardiac Ferritin H Facilitates Cardiomyopathy via Slc7a11-Mediated Ferroptosis. *Circ Res* **127**, 486-501, doi:10.1161/CIRCRESAHA.120.316509 (2020).
36. Rui, T. *et al.* Deletion of ferritin H in neurons counteracts the protective effect of melatonin against traumatic brain injury-induced ferroptosis. *J Pineal Res* **70**, e12704, doi:10.1111/jpi.12704 (2021).
37. Du, J. *et al.* DHA inhibits proliferation and induces ferroptosis of leukemia cells through autophagy dependent degradation of ferritin. *Free Radic Biol Med* **131**, 356-369, doi:10.1016/j.freeradbiomed.2018.12.011 (2019).
38. Zhang, Z., Zhao, M. & Wang, G. Hsa_circ_0051079 functions as an oncogene by regulating miR-26a-5p/TGF-beta1 in osteosarcoma. *Cell Biosci* **9**, 94, doi:10.1186/s13578-019-0355-2 (2019).
39. Wang, J. *et al.* The regulatory effect of has-circ-0001146/miR-26a-5p/MNAT1 network on the proliferation and invasion of osteosarcoma. *Biosci Rep* **40**, doi:10.1042/BSR20201232 (2020).
40. Chen, R., Wang, G., Zheng, Y., Hua, Y. & Cai, Z. Drug resistance-related microRNAs in osteosarcoma: Translating basic evidence into therapeutic strategies. *J Cell Mol Med* **23**, 2280-2292, doi:10.1111/jcmm.14064 (2019).
41. Rastogi, S., Aggarwal, A., Tiwari, A. & Sharma, V. Chemotherapy in Nonmetastatic Osteosarcoma: Recent Advances and Implications for Developing Countries. *J Glob Oncol* **4**, 1-5, doi:10.1200/JGO.2016.007336 (2018).

Figures

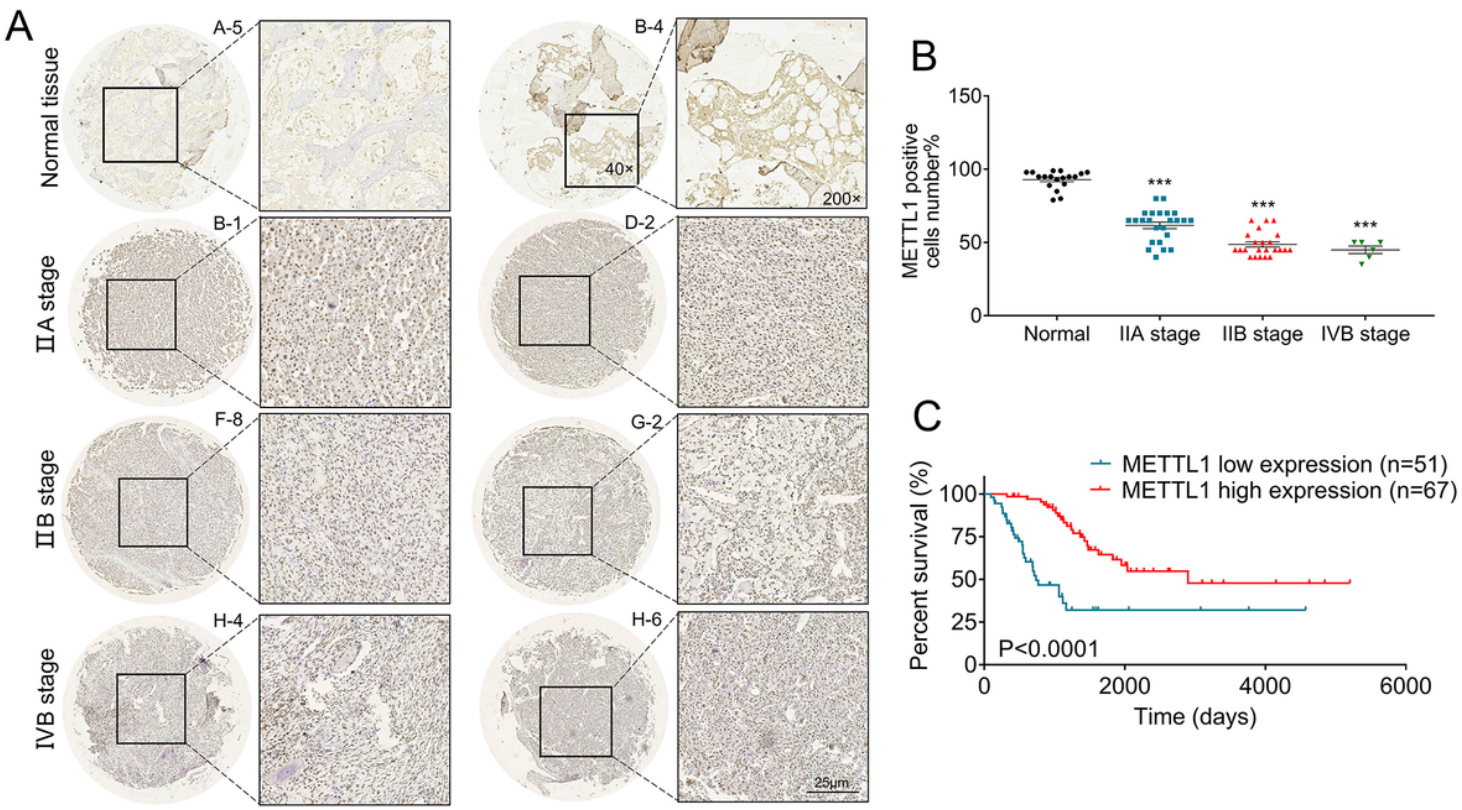

Figure 1

METTL1 expression is decreased in osteosarcoma tissues and has been implicated in patient's survival. (A) Immunohistochemistry (IHC) analysis of METTL1 protein expression on tissue microarrays (TMAs) composed of benign bone tissues (n=20), IIA stage osteosarcomas (n=31), IIB stage osteosarcomas (n=31), and IVB stage osteosarcomas (n=6) tumor cores. Representative IHC images (magnification ×40 and ×200) are presented (Bar: 25 μm). (B) The statistical figure representing the percentages of METTL1 positive cells number. (C) Kaplan–Meier survival curve indicates the difference in survival rate between METTL1 high expression and METTL1 low expression patients. Data were expressed as mean ± SEM.; ***P < 0.001.

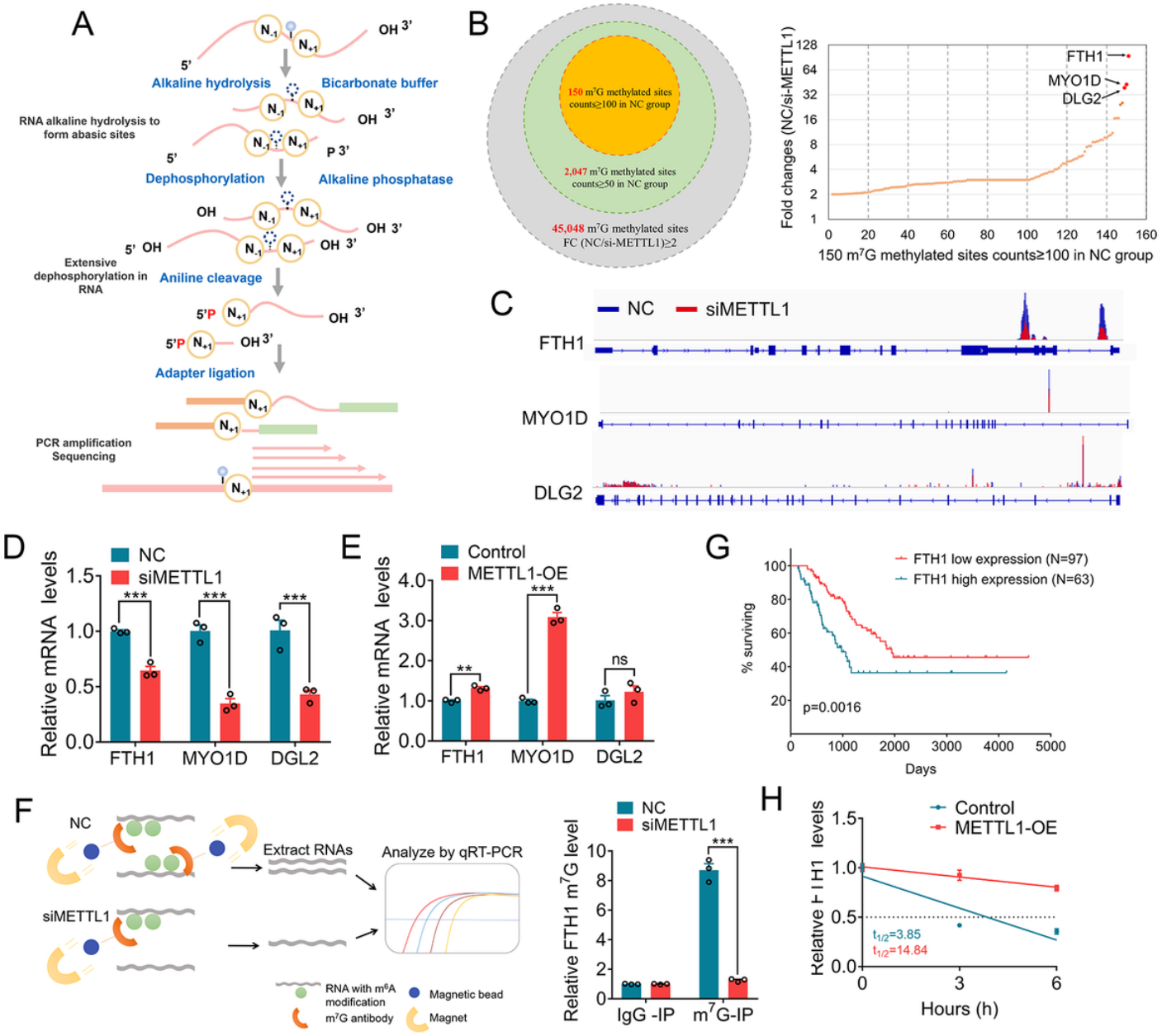

Figure 2

METTL1 increases the m7G methylation modification of FTH1 and promotes the stabilization of FTH1 mRNA.(A-B) Schematic diagram of m7G AlkAniline-seq (A) and sequencing results (B). (C) m7G methylation modification fold change of mRNA detected by gene-specific m7G assay in 143B cells with METTL1 depletion. (D-E) qRT-PCR analysis revealed the expression of FTH-1, MYO1D, and DLG2 after knockdown (D) or forced expression (E) of METTL1. (F) Enrichment of FTH1 by MeRIP-qPCR with m7G antibody decreased in 143B cells after METTL1 silencing. (G) Kaplan-Meier survival curve indicates the difference in survival rate between FTH1 high expression and FTH1 low expression patients. (H) qRT-PCR analysis of the mRNA stability of FTH1 after

the treatment of 10 μg/mL actinomycin D at the indicated time points flowing with overexpression of METTL1 in 143B cells. Data were expressed as mean ± SEM. **P < 0.01; ***P < 0.001.

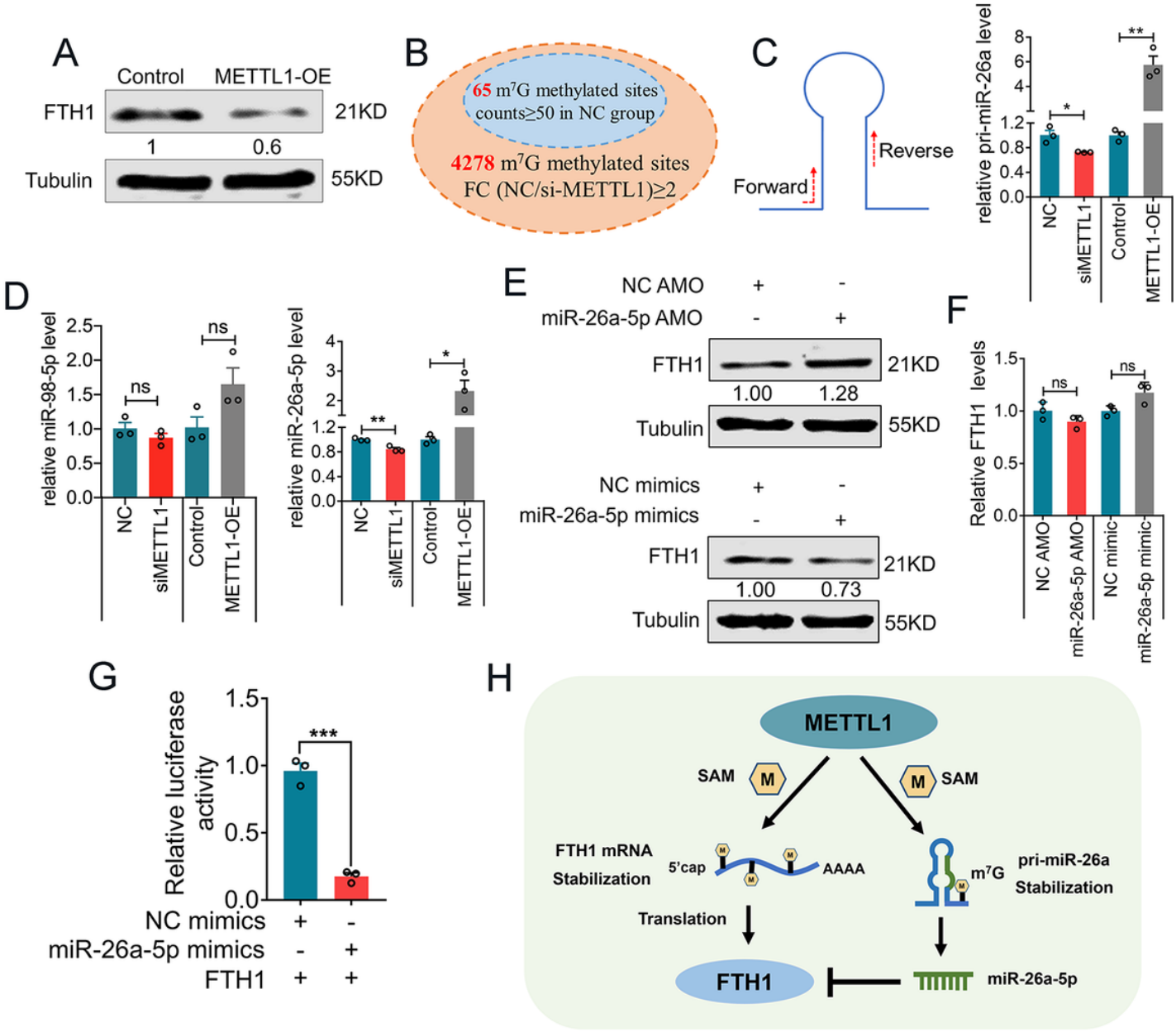

Figure 3

METTL1 decreases FTH1 translation via mediating the mature of miR-26a in an m7G-dependent manner. (A) Western blot analysis of the expression of FTH1 at the protein level with forced expression of METTL1. (B) m7G methylation modification change fold of pri-miRNA detected by m7G AlkAniline-seq in 143B cells with or without METTL1 knockdown. (C) Pri-miRNA schematic (Left); qRT-PCR analysis revealed the function of METTL1 overexpression or knockdown on pri-miR-26a expression (Right). (D) Expression of miR-98-5p (Left) and miR-26a-5p (Right) was measured by qRT–PCR after transfection with si-METTL1 and METTL1 overexpression vectors in 143B cells. (E-F) Expression of FTH1 at protein (E) and mRNA levels (F) after transfection of miR-26a-5p AMO or mimics. (G) Luciferase activity assays were performed to confirm FTH1 mRNA was directly bound to miR-26a-5p in 143B cells. (H) Schematic diagram of METTL1 regulating FTH1 and Pri-miR-26a. Data were expressed as mean ± SEM. *P < 0.05; **P < 0.01; ***P < 0.001.

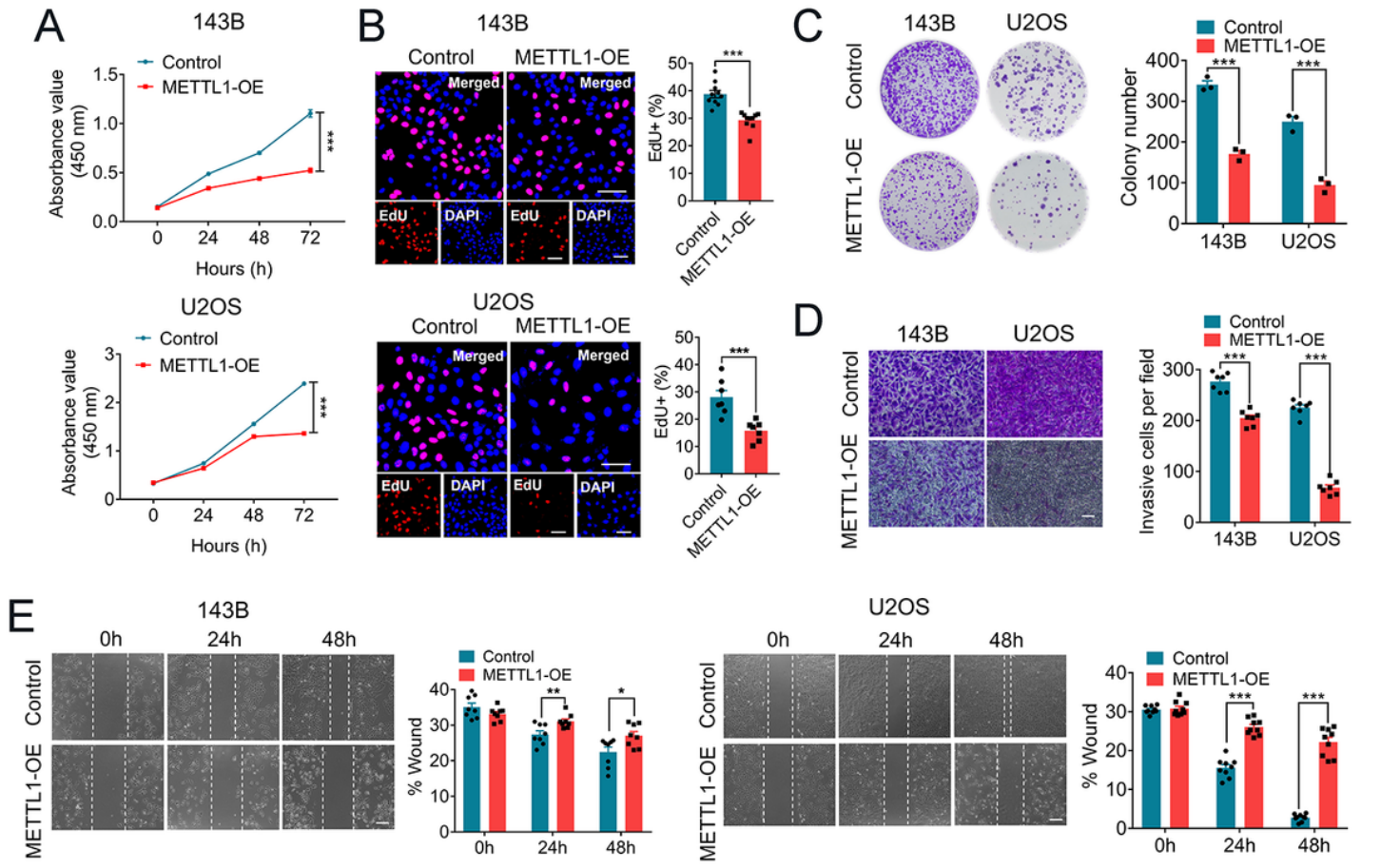

Figure 4

Tumor inhibition impact of METTL1 in human osteosarcoma cells. (A–B) Effects of forced expression of METTL1 expression on cell viability (A) and proliferation (B) in 143B (upper) and U2OS (lower) cells. (Bar: 50 μm). (C) Colony formation assay was performed in 143B (Left) and U2OS (Right) cells with METTL1 overexpression vectors transfection. (D) Invasion assay using Matrigel invasion chamber showed that METTL1 overexpression receded osteosarcoma invasiveness in 143B (Left) and U2OS (Right) cells. (Bar: 100 μm). (E) Migration ability was detected by wound-healing assay at 0, 24, and 48 h respectively with METTL1 overexpression in 143B (Left) and U2OS (Right) cells. (Bar: 100 μm). Data were expressed as mean ± SEM. *P < 0.05; **P < 0.01; ***P < 0.001.

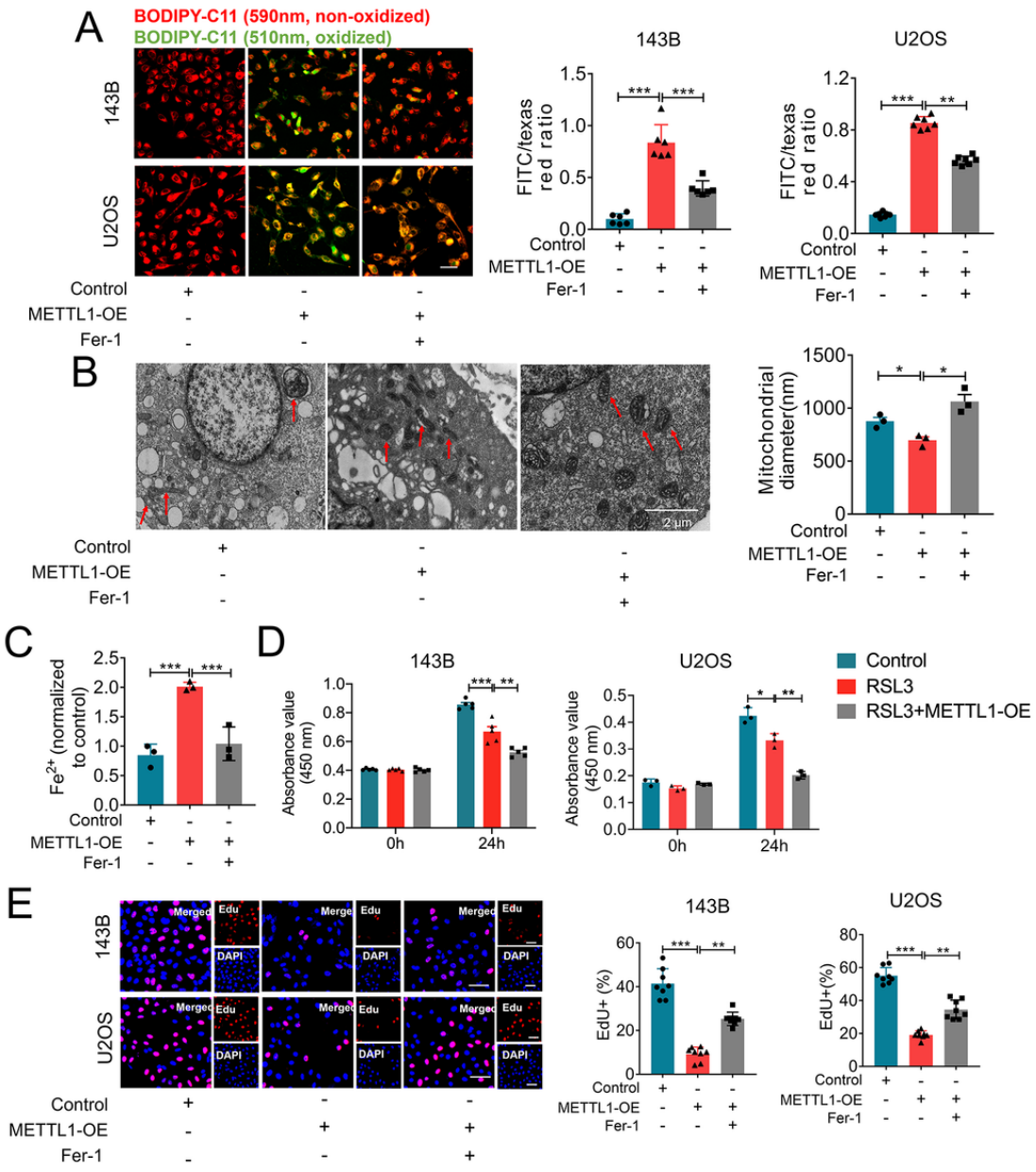

Figure 5

METTL1 promotes the progression of ferroptosis in osteosarcoma cells. (A) The relative level of lipid peroxidation was detected by C11-BODIPY fluorescence after overexpression of METTL1 in 143B (upper) and U2OS (lower) cells. Cells were pretreated with or without 0.5μM for two hours. (Bar: 50 μm). (B) 143B cells morphology was observed via transmission electron microscopy. (Left) The diameter of the mitochondria is the quantitative analysis by using the ImageJ software (Right) (Bar: 2 μm). (C) After 143B cells were pretreated with or without 0.5μM Fer-1 for two hours, cells were transfected with METTL1 overexpressed plasmid, and the relative levels of Fe2+ were assayed. (D) CCK8 assays were performed to determine the cell viability of 143B (left) and U2OS (right) cell lines after METTL1 plasmid transfection, with or without 1μM RSL3 at 24 h. (E) EdU staining showed that Fer-1 reversed the inhibitory effect of METTL1 overexpression on 143B (upper) cells and U2OS (lower) cells proliferation. (Bar: 50 μm). Data were expressed as mean ± SEM. *P < 0.05; **P < 0.01; ***P < 0.001.

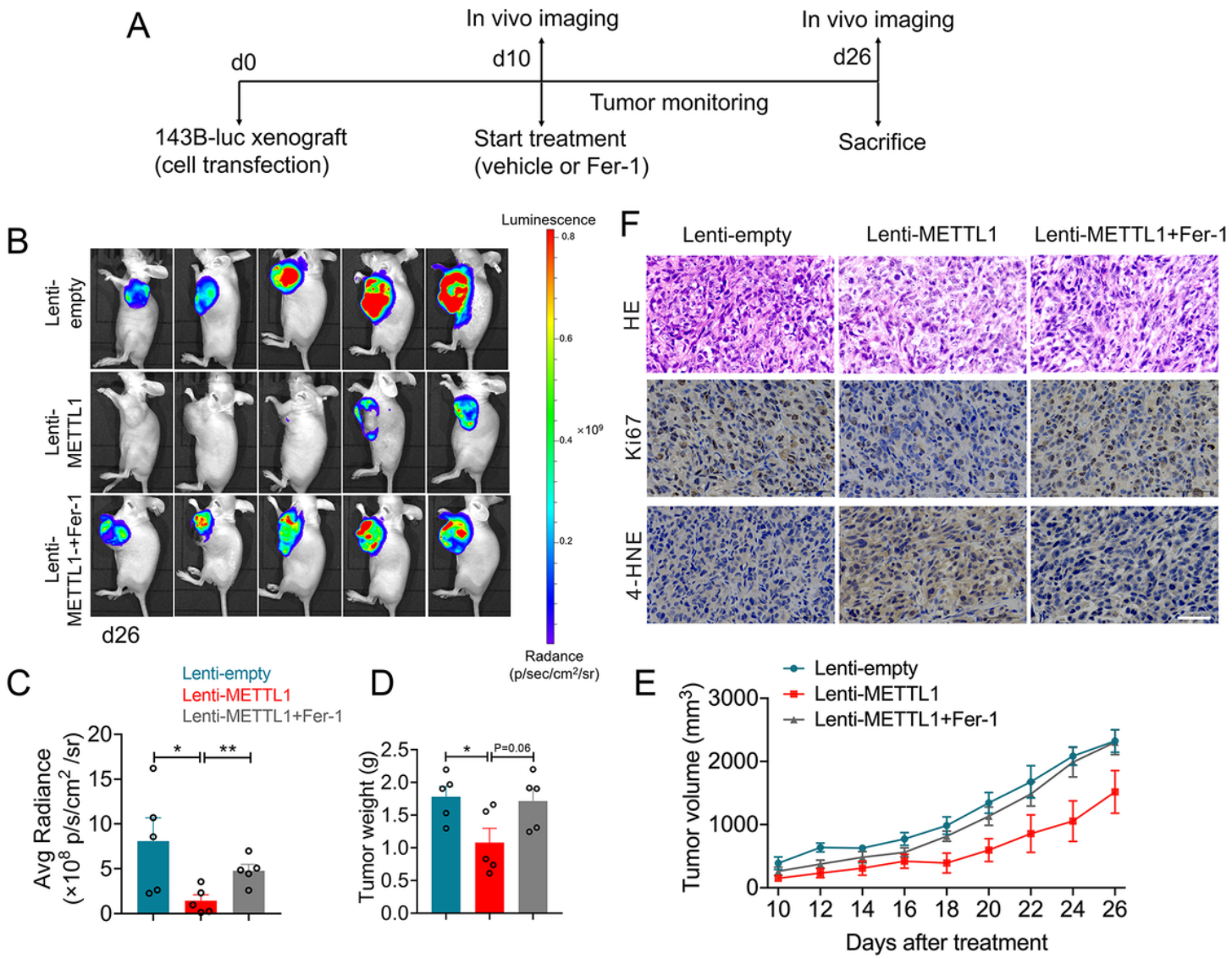

Figure 6

Fer-1 reversed the inhibition effects of METTL1 on tumor growth in vivo. (A) Schematic of Dosing Times for cell line-derived xenograft experiments. Mice underwent in vivo imaging scans on day 10 and treatment was initiated (daily intraperitoneal injections of vehicle or 1 mg/kg Fer-1), and tumors were taken after another in vivo imaging scan on day 26. (B) Tumor growth was monitored using the vivo imaging system. (C) The statistical figure analysis of the Avg Radiance. (D-E) Tumor weight (D) and volume (E) were assessed from xenografts after dissection. (F) Sections of the tumor were stained with ki-67 and 4-HNE antibodies by immunohistochemical assay and H&E staining (Bar: 50 μm). Data were expressed as mean ± SEM. *P < 0.05; **P < 0.01.

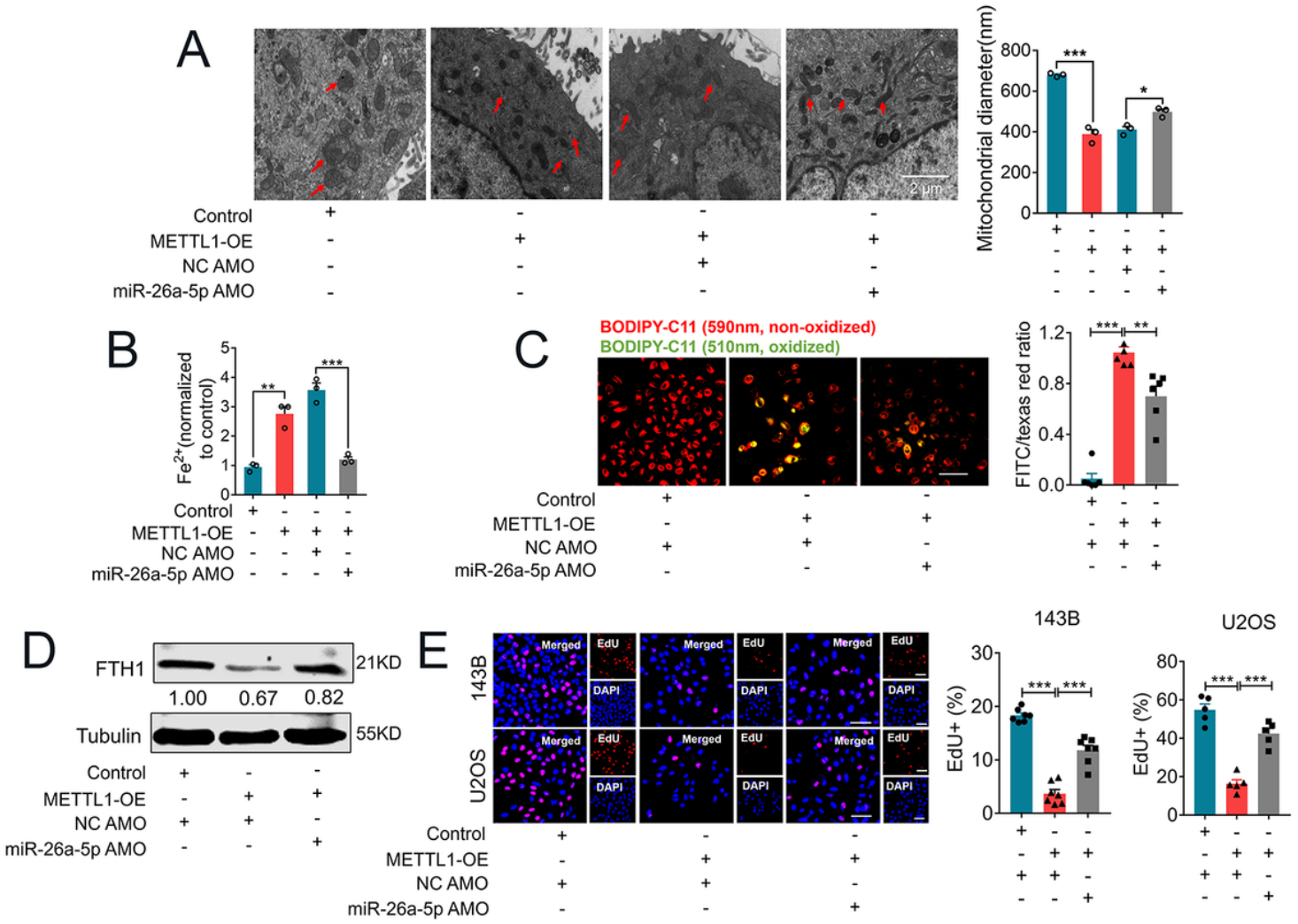

Figure 7

miR-26a-5p AMO reversed the promoting effect of METTL1 on ferroptosis in osteosarcoma cells. (A) 143B cells morphology was observed via transmission electron microscopy (Left). The diameter of the mitochondria is the quantitative analysis by using the ImageJ software (Right, Bar: 2 μm). (B) Iron assay experiments showed that miR-26a-5p AMO reversed the increased iron levels induced by METTL1 forced expression in 143B cells. (C) The relative lipid peroxidation levels were assayed via C11-BODIPY fluorescence in 143B cells. (Bar: 50 μm). (D) The results of western blot analysis showed that miR-26a-5p AMO reversed the reduction of FTH1 protein levels resulting from high METTL1 expression in 143B cells. (E) EdU staining and its statistical diagram showed the reversed effects of miR-26a-5p AMO on proliferation inhibition of METTL1 overexpression in 143B (upper) cells or U2OS (lower) cells. (Bar: 50 μm). Data were expressed as mean ± SEM. *P < 0.05; **P < 0.01; ***P < 0.001.

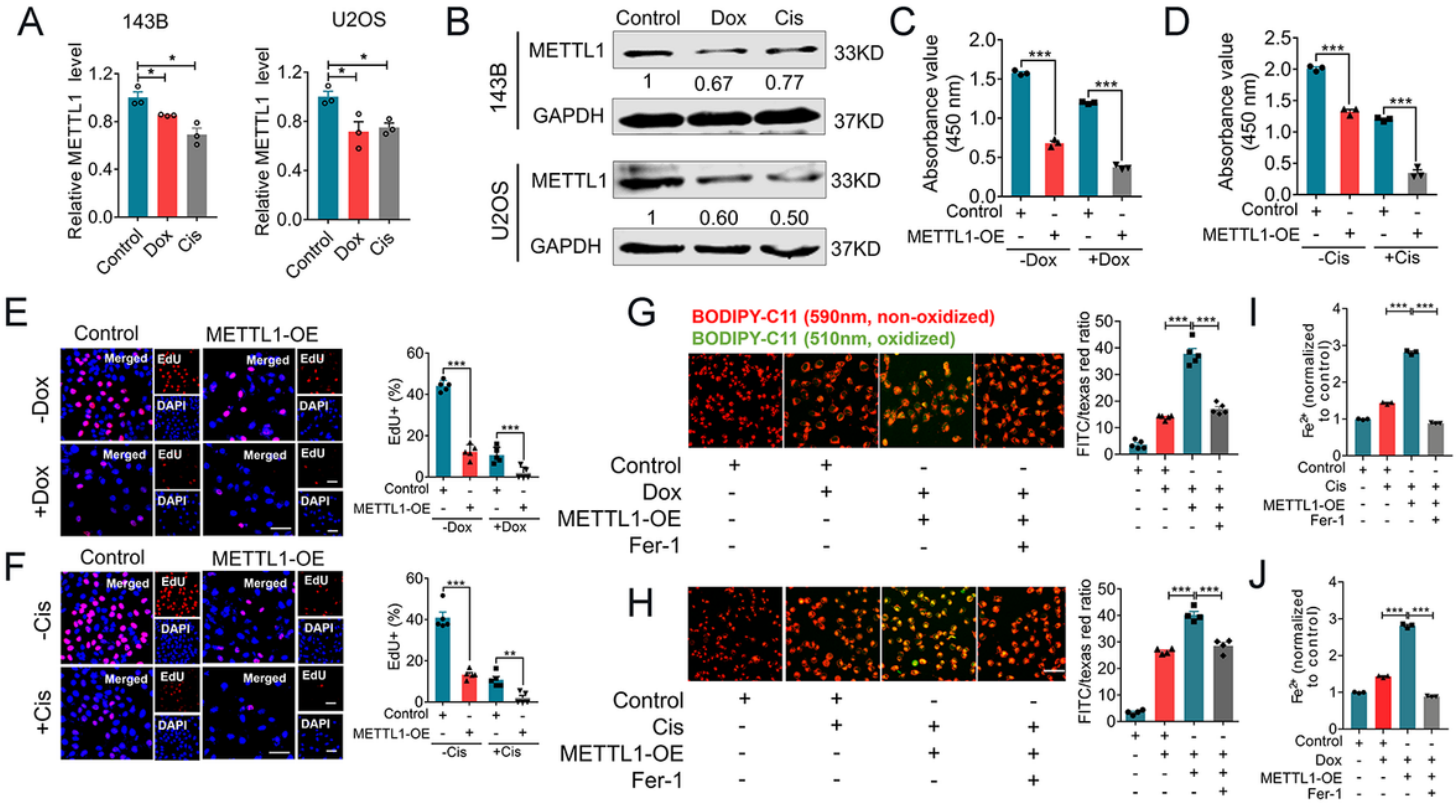

Figure 8

METTL1 increases the sensitivity of osteosarcoma cells to chemotherapeutic agents. (A-B) qRT-PCR (A) and western blot (B) were performed to confirm the expression of METTL1 in 143B and U2OS cells, treated with 0.69 μM doxorubicin or 0.5 μM cisplatin for 24 h. (C-D) 143B cells were treated with 0.69 μM doxorubicin (C) or 0.5 μM cisplatin (D) for 24 h. Cell viability was assessed by CCK8 assays. (E-F) Representative images of EdU staining and its statistical diagram in 143B cells transfected with METTL1 overexpression, cells were treated with 0.69 μM doxorubicin (E) or 0.5 μM cisplatin (F) for 24 h. (Bar: 25 μm). (G-H) 143B cells were transfected with METTL1 overexpression, cells were treated with Fer-1 for 2 h, 0.69 μM doxorubicin (G) or 0.5 μM cisplatin (H) 24 h. Then lipid peroxidation was assessed using BODIPY-C11 staining. (Bar: 50 μm). (I-J) 143B cells were transfected with METTL1 overexpression, cells were treated with 0.5 μM Fer-1 for 2 h, 0.69 μM doxorubicin (I), or 0.5 μM cisplatin (J) for 24 h, the relative levels of Fe2+ were assayed. Data were expressed as mean ± SEM. *P < 0.05; **P < 0.01; ***P < 0.001.

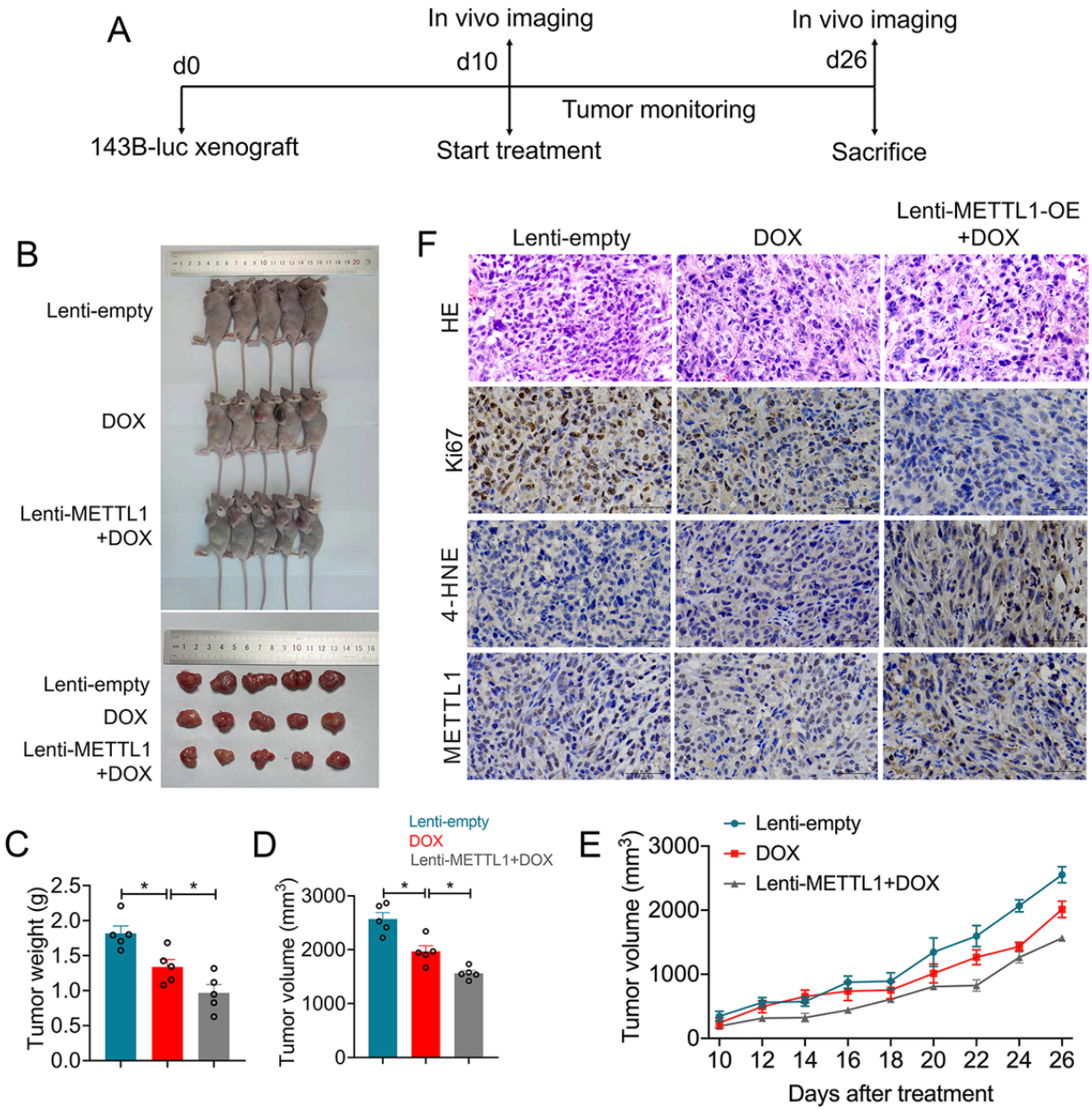

Figure 9

METTL1 inhibited tumor growth and increased the sensitivity to chemotherapeutic agents in vivo. (A) Schematic of Dosing Times for cell line-derived xenograft experiments. Mice underwent in vivo imaging scans on day 10 and treatment was initiated (daily intraperitoneal injections of saline or 1 mg/kg doxorubicin), and tumors were taken after another in vivo imaging scan on day 26. (B) The image showing the comparison of the excised tumor size of 143B xenografts in nude mice. (C-D) Weight (C) and volume (D) of tumor tissues removed from nude mice. (E) Statistics of change in volume of cell line-derived xenograft tumors after treatment. (F) HE and immunohistochemical staining of tumor samples collected from mice at the end of treatments. (Bar: 50 μm). Data were expressed as mean ± SEM. *P < 0.05.

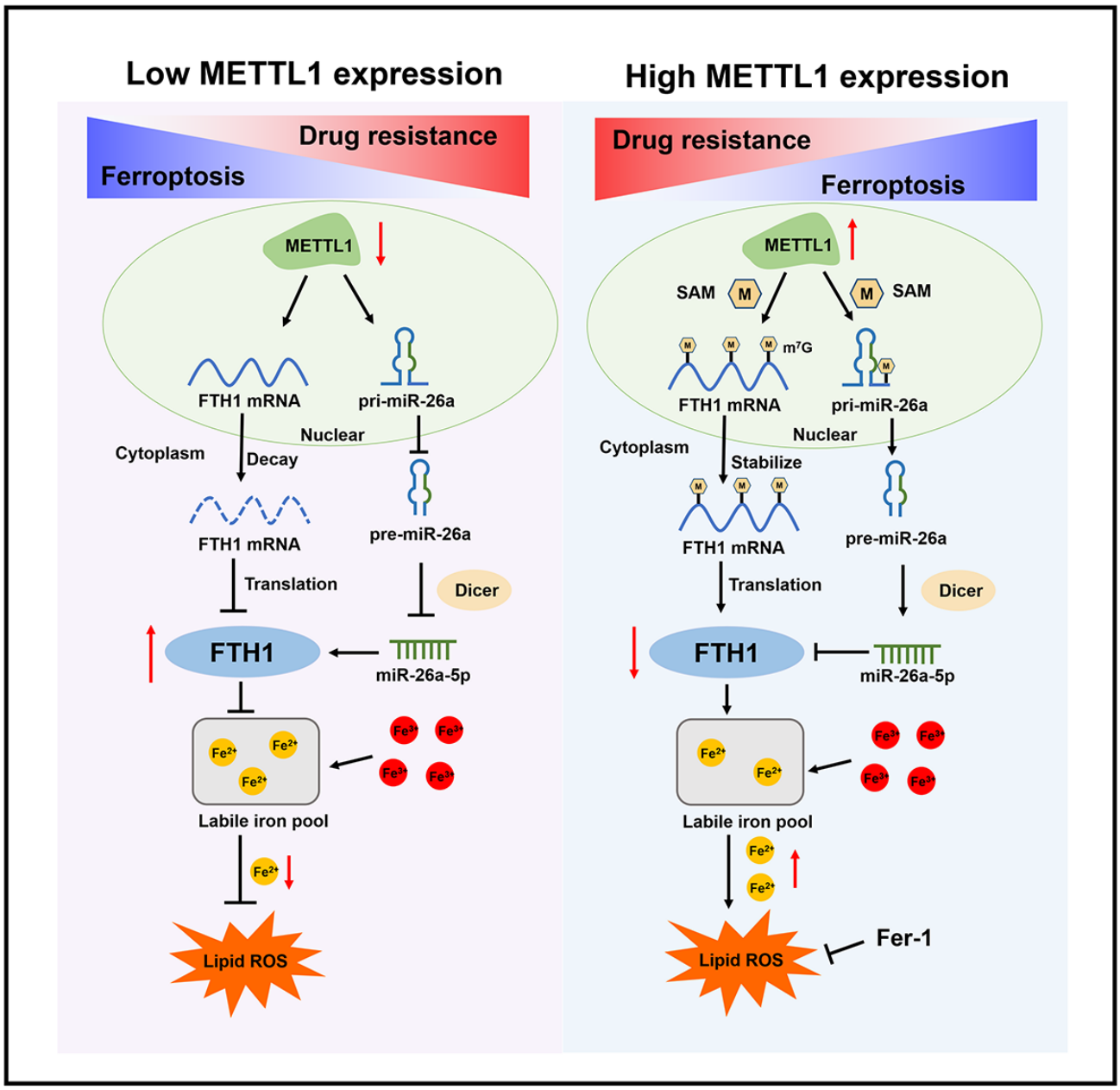

Figure 10

Schematic illustration for the function of METTL1 in ferroptosis and chemotherapy resistance via targeting pri-miR-26a/FTH1 signaling axis in an m7G methylation modification manner in osteosarcoma.

Supplementary Files

This is a list of supplementary files associated with this preprint. Click to download.

- FigureS1.pdf
- FigureS2.pdf
- FigureS3.pdf
- FigureS4.pdf
- FigureS5.pdf
- FigureS6.pdf

- TableS1.pdf